ISSN 0015-4628, Fluid Dynamics, 2024, Vol. 59, No. 2, pp. 331–343. © Pleiades Publishing, Ltd., 2024.
ISSN 0015-4628, Fluid Dynamics, 2024. © Pleiades Publishing, Ltd., 2024.

Numerical and Experimental Studies on Curvature-Induced Behavior of Detonation Waves in an Annular Channel

Z. H. Pan[a], J. Zhou[a], N. Jiang[a], and P. G. Zhang[a,*]

[a]*School of Energy Resources and Power Engineering, Jiangsu University, Zhenjiang, China*

**e-mail: zhangpg@ujs.edu.cn*

Received September 18, 2023; revised December 7, 2023; accepted December 14, 2023

Abstract—To elucidate the influence of curvature on the mechanism governing stable detonation waves, this study delves into the experimental and numerical exploration of gaseous detonations within an annular channel utilizing a $2H_2/O_2/3Ar$ mixture. The investigation encompasses both empirical observations of the cellular structure of the detonation wave through a soot-coated stainless-steel plate and numerical simulations employing advanced methodologies. To capture the intricacies of the detonation phenomenon, the second-order additive semi-implicit Runge–Kutta method and the fifth-order weighted essentially non-oscillatory (WENO) scheme are adeptly employed for discretizing the time and spatial derivatives, respectively. The underlying chemical reactions during detonation are meticulously modeled using a detailed reaction mechanism. The pressure and velocity contours unveiling a nuanced picture are extracted using a numerical analysis. The inner wall divergence effect emerges as a critical determinant, weakening the detonation strength and consequently yielding the larger cellular structures. Contrarily, the outer wall convergence effect significantly amplifies the strength yielding the smaller cellular structures. This intricate interplay causes the detonation velocity to increase progressively along the radial direction. Furthermore, near the inner wall the detonation wave manifests periodic phases of augmentation and attenuation, resulting in oscillations in both the velocity and the pressure. A granular scrutiny of the flow field finer attributes underscores the continuous regeneration and dissolution of triple points along the wave front. Notably, triple point regeneration predominantly occurs near the outer wall surface, while their dissipation is more proximate to the inner wall. In the context of the stable detonation wave, equilibrium between triple point regeneration and decay sustains a constant triple point count on the wave front. This pivotal equilibrium enables the self-sustaining propagation of detonation within the annular channel.

Keywords: annular channel, stable propagation, triple point, cellular structure, periodic variation

DOI: 10.1134/S0015462823602255

Hydrogen combustion produces water as its main byproduct, making hydrogen energy to be a highly promising clean energy source in the 21st century. The hydrogen energy investigations have been extensively conducted worldwide since the 1970s. However, there exists a notable gap in comprehensive knowledge concerning hydrogen, particularly in terms of safety concerns related to its storage, transportation, and utilization. This study focuses on the secure transportation of hydrogen within tubes during industrial production processes. The electrostatic forces or unidentified factors, especially within the annular section of tube connections, can lead to ignition incidents, potentially resulting in propagation of a detonation wave. On the other hand, a new type of power propulsion system known as the Continuous Rotating Detonation Engine features an annular combustion chamber structure. Smirnov et al. [1, 2], Betelin et al. [3], and Nikitin et al. [4] demonstrated the propagation of detonation waves within it through three-dimensional modeling of rotating detonation in pulse jet engines. In this case, it is noteworthy that within annular combustion chambers, the occurrence of Mach reflection along the outer wall of the tube intensifies the detonation wave, subjecting the outer wall to exceptionally high pressure loads and potential vulnerability [5–7]. Consequently, the thorough investigation of the detonation phenomenon in the specific geometry of annular combustion chambers becomes imperative.

The well-established fact is that the detonation wave converges near the concave wall, rendering it more robust as compared to its counterpart near the divergent convex wall [8]. Consequently, the detonation strength distribution along the detonation front becomes non-uniform [9–12]. As a result, stabilized detonation waves can propagate consistently through annular channels while maintaining a distinct

curved shape [13–15]. This shape of the shock wave front demonstrates self-similarity for equivalent values of r_i/λ, where r_i represents the curvature radius of the inner wall and λ denoted the normal detonation cell width. This characteristic holds true regardless of the annular channel specifics and the gas mixture employed [16]. However, when the curvature radius or the initial pressure falls below a critical threshold, the detonation wave propagates in unstable manner [17–19]. Numerical and experimental findings indicate that under near-limit conditions, cellular structures exhibit periodic variations that include regeneration, reduction, and partial or complete disappearance [20, 21]. These variations arise from expansion waves leading to a localized failure of the transverse structure and, consequently, the detonation process. This phenomenon causes cellular structures near the inner wall to enlarge or even vanish [22, 23]. Subsequently, overdriven detonation could potentially occur via local explosions or Mach reflections near curved channel walls. Thus, three regimes of detonation propagation are observable in annular channels, namely, the stable, transitional, and unstable regimes. Transition from unstable to stable propagation occurs at approximately $14 \le r_i/\lambda \le 23$ [16].

As the transverse wave emerging from the triple point in the Mach configuration propagates laterally along the detonation front, it supports the primary detonation wave and contributes to the cellular structure. The natural transverse spacing is directly related to the λ and is influenced by the flow fields and the detonation strength [24]. Given the boundary conditions, the cellular structure is solely dependent on the initial conditions of the mixture. In [25] it was discussed how various ignition source positions during the detonation initiation initially cause irregularities in the cellular structure. With time, the structure becomes more uniform despite the initial irregularities and the system "forgets" the initial non-uniformity of ignition sources. In [26] it was further explored, by means of detonation simulations, how various factors such as the gas temperature and the channel width affect the cell structure during detonation, influencing the behavior and size of the detonation waves. However, from the preceding discussion it is evident that the detonation wave is significantly affected by both the expansion waves near the inner wall and the compression effects near the outer wall. When the divergence effect originating from the inner wall impacts the local wave front, the triple point intensity diminishes or even disappears. Consequently, near the inner wall λ increases, causing pronounced curvature of the detonation front and eventually leading to local quenching near the inner wall. Conversely, near the outer wall the compression effect enhances the shock wave strength resulting in the relatively smaller λ. This effect supports self-sustained detonation propagation and establishes a dynamic balance. The disruption of this balance, due to the reduced inner radius or initial pressure, leads to transition from stable to unstable detonation propagation [15]. However, the conclusive evidence is yet to emerge regarding how these positive and negative effects precisely influence stable detonation.

The present study delves into the impact of curvature on detonation propagation within annular channels by means of both experimental and numerical analysis. We provide experimental cellular structure data across various initial pressures to analyze the behavior of diverse detonation propagations. To elucidate the self-sustained propagation mechanism of detonation waves within the annular channels, we conduct an intricate analysis of the detonation wave flow field, the pressure evolution, and variations in the triple point strength.

1. EXPERIMENTAL SETUP

In Fig. 1 we have reproduced the experimental configuration designed for studying detonation wave propagation within an annular channel. The experimental apparatus encompasses distinct sections, namely a 1000-mm driven straight section I, a 2580-mm driven straight section II, a 180-degree annular test section III, and a 1300-mm extended straight section IV. These sections are meticulously fabricated from polycarbonate plates. To facilitate the introduction of different premixed mixtures, sections I and II are separated by an aluminum film. The channel cross-section is uniform and rectangular, measuring 30 mm × 4 mm. Notably, the annular channel features inner and outer wall radii of curvature measuring 70 and 100 mm, respectively.

A detonation is initiated using a stoichiometric C_2H_4–O_2 mixture possessing a high initial pressure ($p_0 = 80$ kPa) in section I, which serves as the driver mixture. To trigger the premixed mixture of $2H_2$–O_2–3Ar in section I, a high voltage spark probe (with an ignition voltage of 5 kV) is positioned on the end wall of the section. Upon ignition, an overdriven detonation wave penetrates through the aluminum film into section II, where direct initiation of detonation transpires. This is succeeded by relaxation into a steadily propagating detonation wave before entering section III. Subsequently, the detonation wave advances through section II, followed by the section III that constitutes an equivalent rectangular cross-section annular channel.

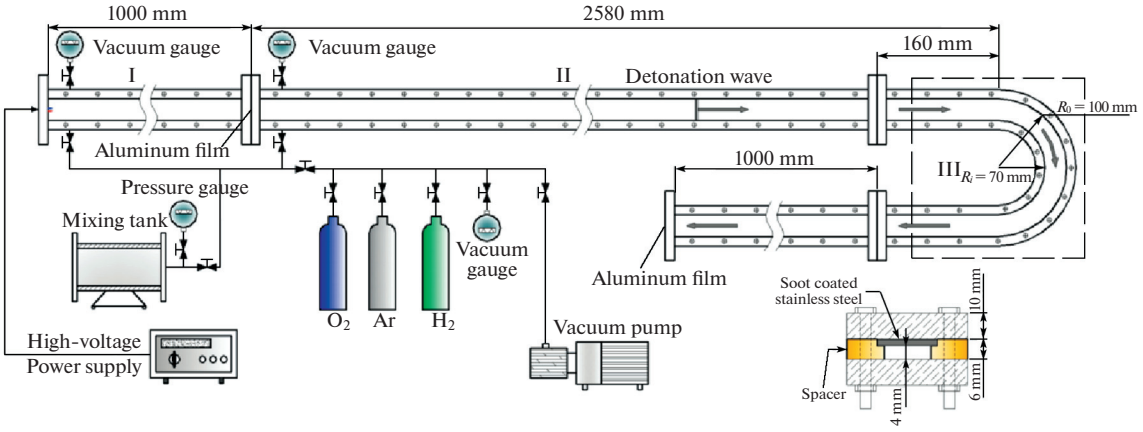

Fig. 1. Sketch of the experimental arrangement used in studying the curvature-induced behavior of detonation tests.

In each experimental trial, the pre-evacuated channel is charged with a $2H_2-O_2-3Ar$ mixture to attain the desired pressure p_0. The monitoring of p_0 is facilitated by the precise digital vacuum gauge (OMEGA HHP 242-015A, 0-15 psi), boasting an accuracy of $\pm 0.10\%$ of its full scale. Gas is thoroughly mixed in the tank through the partial pressure for a minimum of 24 h to ensure homogeneity before being introduced into the channel. For various $2H_2-O_2-3Ar$ mixtures, the Chapman–Jouguet (CJ) detonation velocities (D_{CJ}) are computed employing the Gorden–McBride code [27]. Discussing the methodology for measuring detonation cell size is relevant. A standard technique for obtaining cellular structures involves using side wall soot records, which capture the trajectories of Mach intersection points on the walls. Side wall soot records cover a certain distance along the detonation front. Observing the detonation from a farther distance greatly aids in identifying the predominant cell sizes. Obtaining a single representative value for cell size from the irregular soot foil pattern is not an easy task. There exists a distribution of cells of various sizes on the soot plate, further complicated by the fine structure of higher harmonic waves embedded within the cells. To achieve the consistent results, we have measured cells at various positions on the soot foil (at the same radial location) and averaged them, aiding in providing reliable values that characterize the cell sizes for a specific mixture. Considering human factors and measurement instrument precision, the error range in cell size measurements here does not exceed 10%.

2. PHYSICAL AND NUMERICAL MODELS

2.1. Governing Equation and Numerical Method

The two-dimensional chemical non-equilibrium Euler equations, formulated in the non-dimensional and generalized body-fitted coordinates (ξ, η), can be expressed as follows:

$$\frac{\partial \mathbf{U}}{\partial t} + \frac{\partial \mathbf{F}}{\partial \xi} + \frac{\partial \mathbf{G}}{\partial \eta} = \mathbf{S}, \tag{2.1}$$

where

$$\mathbf{U} = \{\rho_1, \rho_2, \ldots, \rho_K, \rho u, \rho v, E\}^T,$$

$$\mathbf{F} = \left\{\rho_1 \bar{U}, \rho_2 \bar{U}, \ldots, \rho_K \bar{U}, \rho u \bar{U} + p\xi_x, \rho v \bar{U} + p\xi_y, \bar{U}(p+E)\right\}^T,$$

$$\mathbf{G} = \left\{\rho_1 \bar{V}, \rho_2 \bar{V}, \ldots, \rho_K \bar{V}, \rho u \bar{V} + p\eta_x, \rho v \bar{V} + p\eta_y, \bar{V}(p+E)\right\}^T,$$

$$\mathbf{S} = \{\dot{\omega}_1, \dot{\omega}_2, \cdots, \dot{\omega}_K, 0, 0, 0\}^T,$$

$$\bar{\mathbf{U}} = u\xi_x + v\xi_y,$$

$$\bar{\mathbf{V}} = u\eta_x + v\eta_y.$$

Here, u and v are the velocity components in the physical coordinates (x, y), ρ denotes the mixture density given by the relation $\rho = \sum_{k=1}^{K} \rho_k$, where $\rho_k = \rho Y_k$ and Y_k is the mass fraction of the kth species,

p denotes the pressure, and E is the total energy per unit volume, calculated as $E=\rho\sum_{k=1}^{K}Y_k e_k+\rho(u^2+v^2)/2$, where e_k being the internal energy of the kth species per unit mass. The mass production rate of the kth species, denoted as $\dot{\omega}_k$, is given by Eq. (2.2)

$$\dot{\omega}_k = W_k\sum_{j=1}^{\mathrm{NR}}(v''_{kj}-v'_{kj})\left(k_{fj}\prod_{k=1}^{\mathrm{ns}}n_k^{v'_{kj}}-k_{bj}\prod_{k=1}^{\mathrm{ns}}n_k^{v''_{kj}}\right), \tag{2.2}$$

where NR is the number of elementary reactions, ns is the number of species, v'' and v' are the stoichiometric coefficients for the reactant and the product, respectively, W_k is the molecular weight, n_k is the mole concentration of the kth species, and k_{fj} and k_{bj} are the rate coefficients for the forward and reverse reactions, respectively.

To mitigate the physical oscillations and excessive numerical dissipations that may arise from high−resolution requirements for the fine flow field structures, the spatial derivatives of the inviscid fluxes **F** and **G** in Eq. (2.1) are discretized using the fifth-order weighted essentially non-oscillatory (WENO) scheme [28].

For simplicity of WENO presentation, the one-dimensional convective problem is discussed based on the following equation

$$\frac{\partial U}{\partial t}+\frac{\partial F}{\partial \xi}=0. \tag{2.3}$$

The flux vector **F** can be split as follows:

$$F_j=F_j^{+}+F_j^{-}=A^{+}U+A^{-}U, \tag{2.4}$$

where **A** is the Jacobian matrix, $\mathbf{A}=\dfrac{\partial F}{\partial U}=R\Lambda R^{-1}=A^{+}+A^{-}$ and Λ is the diagonal matrix with the eigenvalues on the diagonal. The eigenvalues are positive in A^{+} and negative in A^{-}. From Eq. (2.3) we have

$$\frac{\partial q}{\partial t}+\frac{\partial f}{\partial \xi}=0, \tag{2.5}$$

where $q=R^{-1}U$ and $f=R^{-1}F$. In terms of the Law−Friedrichs splitting

$$f_j^{\pm}=\frac{1}{2}(f_j\pm\max_q|\Lambda|q_j), \tag{2.6}$$

where the maximum is taken over the relevant range of q.

In order to get adequate the flux vectors on the cell boundaries, i.e., $f^{\pm}_{j+1/2}$, which would be the key to solve Eq (2.5), the fifth-order WENO scheme is employed. Given a location of jth cell, an interpolation stencil covering k cells is defined by the relation

$$S^r(j)=\{I_{j-r},...,I_{j+s}\},$$

where r is cell shift to the left, s is the right shift, and $r+s+1=k$. Then we have

$$f_{j+1/2}^{\pm(r)}=\sum_{i=0}^{k-1}C_{ri}f_{j-r+i}^{\pm}, \tag{2.7}$$

where the constants C_{ri} are given and listed in [28].

Instead of using only one stencils, three candidate stencils are used in the fifth-order WENO scheme, namely,

$$S^r(j)=\{I_{j-r},\cdots,I_{j-r+2}\}\, r=0,1,2. \tag{2.8}$$

Then taking a convex combination of all $f_{j+1/2}^{\pm(r)}$ defined in Eq. (2.7) for each stencil in the WENO reconstruction, we obtain

$$f_{j+1/2}^{\pm}=\sum_{r=0}^{2}\omega_r f_{j+1/2}^{\pm(r)}. \tag{2.9}$$

When the function has a discontinuity in the stencil S^r, the corresponding weigh ω_r should be essentially zero, to eliminate the spurious oscillations near the discontinuity in calculations, which leads to the following form of weights [28]:

$$\omega_r = \frac{a_r}{\sum_{s=0}^{k-1} \alpha_s}, \tag{2.10}$$

where

$$\alpha_r = \frac{d_r}{(10^{-6} + \beta_r)},$$

$$d_0 = 3/10, \quad d_1 = 3/5, \quad d_2 = 1/10,$$

$$\beta_0 = \frac{13}{12}\left(f_j^{\pm} - 2f_{j+1}^{\pm} + f_{j+2}^{\pm}\right)^2 + \frac{1}{4}\left(3f_j^{\pm} - 4f_{j+1}^{\pm} + f_{j+2}^{\pm}\right),^2$$

$$\beta_1 = \frac{13}{12}\left(f_{j-1}^{\pm} - 2f_j^{\pm} + f_{j+1}^{\pm}\right)^2 + \frac{1}{4}\left(f_{j-1}^{\pm} - f_{j+1}^{\pm}\right)^2,$$

$$\beta_2 = \frac{13}{12}\left(f_{j-2}^{\pm} - 2f_{j-1}^{\pm} + f_j^{\pm}\right)^2 + \frac{1}{4}\left(f_{j-2}^{\pm} - 4f_{j-1}^{\pm} + 3f_j^{\pm}\right)^2.$$

Hence, the WENO scheme based on Eq. (2.9) is a uniformly high order accuracy and non-oscillatory scheme for the problem containing discontinuities.

The second-order additive semi-implicit Runge–Kutta method [29] is used to discretize the time term and manage the stiffness of the chemical source terms.

$$[I - \Delta t a_1 J(Q^n)]K_1 = \Delta t[f(Q^n) + S(Q^n)], \tag{2.11}$$

$$\left[I - \Delta t a_2 J\left(Q^n + c_{21}K_1\right)\right]K_2 = \Delta t\left[f\left(Q^n + b_{21}K_1\right) + S\left(Q^n + c_{21}K_1\right)\right], \tag{2.12}$$

$$Q^{n+1} = Q^n + \omega_1 K_1 + \omega_2 K_2, \tag{2.13}$$

where $f(Q) = -(\partial F/\partial\xi + \partial G/\partial\xi)$, $J = \partial S/\partial Q$, I is the identity matrix, K_1 and K_2 are the intermediate variable matrixes, Δt is the time step, $a_1 = 1/4$, $a_2 = 1/3$, $b_{21} = 1$, $c_{21} = 5/12$, and $\omega_1 = \omega_2 = 1/2$.

2.2. Computational Model

The physical domain, delineated between two concentric circles with dimensionless radii 0.7 and 1.0, is illustrated in Fig. 2a. In [30, 31] the limitations of error accumulation in supercomputer simulations of unsteady gas dynamic work cycles were studied. The results indicate that while the smaller time steps are required for the entire simulation process, the coarser grid computations accumulate errors more rapidly. The reliability of results increases with enhancement of grid resolution and scheme accuracy but decreases with increase in physical time of the study process. Hence, a fixed 300 × 4840 grid system, with the grid dimensions of 0.1 × 0.1 mm is utilized. The grid is finer than the 0.15 × 0.235 mm grid size employed in [32]. The calculations were executed in a computational window shown in Fig. 2, which partially covers the computational domain and moves along with the detonation wave. Considering the outer and inner wall surfaces as slip, the adiabatic solid condition is defined by Eq. (2.14):

$$\left.\frac{\partial(\bar{U}/\xi)}{\partial\xi}\right|_w = 0, \quad \bar{V}|_w = 0, \tag{2.14}$$

which depends on the wall curvature. In Eq. (2.14) the ratio $\bar{U}/\xi$ represents the angular velocity. Due to stable propagation of the detonation wave, its angular velocity remains consistent, resulting in a gradient of zero in the radial direction for the angular velocity.

The straight channel section is tangential to the annular section, and an initial self-sustained cellular detonation wave is established within the straight channel section. When initiating the calculation, the steady detonation wave smoothly transits into the annular section. The intricate chemical reaction mechanism employs an 8-component model (H, O, H_2, OH, H_2O, O_2, HO_2, and H_2O_2) [33] with the 48-step elementary reaction scheme, and the thermodynamic data are sourced from the JANAF tables [27].

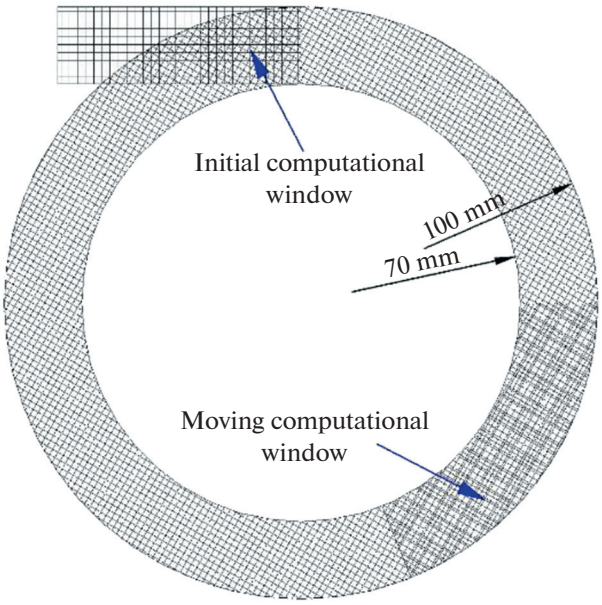

Fig. 2. Schematic diagram of the computational domain.

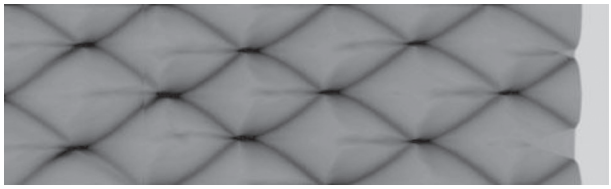

Fig. 3. Numerical cellular structure in the straight tube.

2.3. Numerical Validation

To verify the accuracy of the calculations, this study was aimed to compare the results with the numerical computations [32] and we have performed a basic comparison to validate the computed detonation wave speed with Eckett's experimental results [34].

For direct comparison with the results of computations [32], in the present study we have used identical computational domain and initial conditions: a premixed $H_2/O_2/Ar$ gas mixture in a straight tube with a ratio of 2 : 1 : 3 was considered and the starting pressure and the temperature of 8 kPa and 298 K, respectively, were taken. In Fig. 3 we have given the computed cell images from this study, while in Table 1 we have compared the results obtained in the present study with those from [32]. The computed cell size in the present study is approximately equal to 54 × 30 mm, which closely aligns with Oran's computed size [32] of 54 × 31 mm under the same conditions. The aspect ratio of the cells is equal to 0.556, in good agreement with the experimental aspect ratio of 0.54 obtained in [34]. The propagation speed of the detonation wave is equal to 1589 m/s, exhibiting an error within the 2% range as compared to the theoretical CJ detonation velocity (1617 m/s) computed by the Gordon–McBride program. However, it is more consistent with the experimental detonation wave speed (1550 m/s) obtained in [34]. Therefore, this study's numerical simulations replicate the computations presented in [32] and exhibit consistency with the experimental results from [34].

Table 1. Comparison between the current and Oran et al. results [32] for self-sustaining detonation waves

Study	Grid size	Δx, mm	Δy, mm	Average speed, ms^{-1}	Cell size W (mm) × L (mm)
Current study	2048 × 256	0.1	0.1	1595	30 × 54
Oran et al. [32]	2048 × 256	0.15	0.235	1625	31 × 54

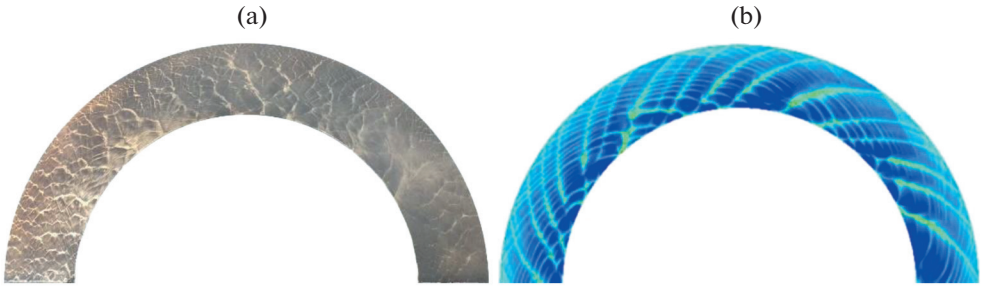

Fig. 4. Cellular structure formed by detonation wave in the annular channel at the initial pressure of 60 kPa. (a) Experimentally measured; (b) numerical simulation.

3. RESULTS AND DISCUSSION

Figure 4a gives the experimental representation of the cellular structure formed by the clockwise-propagating detonation wave navigating the annular channel under the initial pressure condition of 60 kPa. Remarkably, in the immediate neighborhood of the channel entrance, the influence of the curved wall on the detonation wave front appeared negligible, resulting in the emergence of uniform cell sizes denoted by λ. As the detonation wave proceeded along the channel, a discernible expansion of λ near the inner wall was observed, juxtaposed with a concurrent reduction in cell size near the outer wall. This intriguing mechanism behind the formation of cellular structures intricately links to spacing of transverse waves propagating along the wave front, a crucial determinant governing the characteristic parameter λ. The localized divergence effect stemming specifically from the inner wall played the pivotal role in diminishing the intensity of the detonation wave, consequently yielding an augmented spacing between transverse waves. In contrast, the contraction area along the outer wall induced a state of overdriven detonation, consequently narrowing the spacing between transverse waves. The dynamic equilibrium within the channel arises from the intricate interplay between these opposing effects, where the equilibrium position is notably influenced by the curvature and the initial pressure [15]. Crucially, the computed cellular structure illustrated in Fig. 4b exhibits a remarkable qualitative resemblance to the observed experimental results depicted in Fig. 4a, affirming the consistency between the outcomes derived from experimental observations and numerical simulations.

The curvature effect induced by the annular channel introduces a non-uniformity in the strength of detonation wave front. Guided by the shock-change equation

$$\left(\frac{dp}{dt}\right)_s = \frac{\rho a_f^0 \left(\Sigma - \eta \dfrac{\partial u}{\partial x}\right)}{1 + \rho_0 D \left(\dfrac{du}{dp}\right)_S}, \tag{3.1}$$

where $(dp/dt)_s$ denotes the rate of shock pressure change with time, $(du/dp)_s$ signifies the rate of particle velocity change with pressure along the Hugoniot curve for the unreacted material, and a_f stands for the sonic speed of the unreacted material. The density is denoted by ρ, and $\eta = 1 - M_S^2$, where $M_S = D/a_f$. Here, M_S and D, respectively, denote the Mach number and the propagation velocity of the shock wave. In the numerator, the term Σ relates to the net rate at which chemical bond energy is released into the flow through chemical relations, while $\eta(\partial u/\partial x)$ pertains to the rate at which the energy is transported downstream by flow. Since in the adiabatic shock wave $(dp/dt)_s > 0$, the sign of $(du/dp)_s$ is determined by $[\Sigma - \eta(\partial u/\partial x)]_s$. In the context of an adiabatic shock wave in an inert medium, $\Sigma = 0$, yielding:

$$\operatorname{sgn}\left(\frac{dp}{dt}\right)_s = \operatorname{sgn}\left(-\eta \frac{du}{dx}\right)_s. \tag{3.2}$$

Given that $\eta > 0$, when $(\partial u/\partial x) > 0$ (indicative of fluid expansion post-wave), the strength of the shock wave will diminish, and the energy will transfer to the post-wave.

If the flow field beyond the wave sustains $(\partial u/\partial x) = 0$ due to piston-induced compression, the shock wave can propagate steadily. Here, Σ is intricately linked to the chemical reaction. In the case of exothermic reactions with growing molarity, we have $\Sigma > 0$. This phenomenon can bolster the shock wave

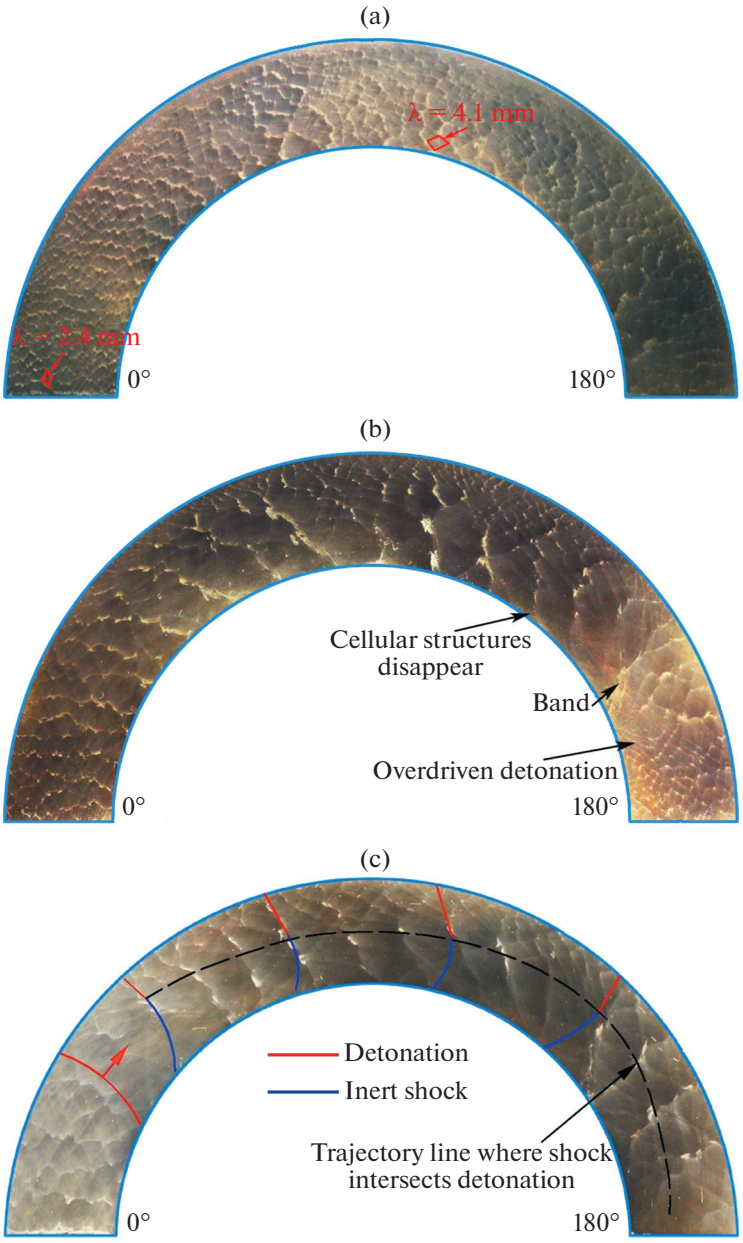

Fig. 5. Experimentally measured cellular structures under the initial pressures of 70 (a), 45 (b), and 30 kPa (c).

strength, implying that a portion of the chemical reaction's heat is utilized to support the shock wave propagation. For the annular channel, the outer wall serves as a converging surface, which exerts a compressive influence on the flow field. This compression leads to a notable escalation in the chemical reaction rate. Consequently, the rapid surge in the chemical reaction rate effectively amplifies the strength of detonation wave in this region, resulting in reduced λ. Conversely, the convex diverging nature of the inner wall engenders the expansion effect on the flow field, yielding a weaker detonation wave and larger λ. Considering the combined effect of divergence and convergence for the inner and outer walls, λ continuously decreases along the radial direction, while the strength of the detonation wave front steadily intensifies. Whether near the inner or outer wall, the circumferential direction maintains a relatively uniform λ, signifying that the detonation wave strength remains fairly.

Figures 5a, 5b, and 5c illustrate the experimental cellular structures observed within the annular channel under varying the initial pressure conditions with the clockwise-propagating detonation waves. In Fig. 5a, as the detonation wave penetrates the annular section, a uniform λ with the width of

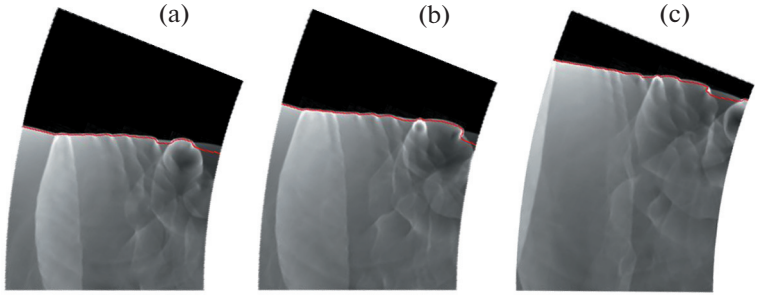

Fig. 6. Numerical simulation of the contours of pressure for the detonation flow field at various instants: $t = 287.43$ (a), $t = 287.71$ (b), and $t = 288$ μs (c).

2.4 mm is evident at the initial pressure of 70 kPa. This λ is comparable to that observed in the straight channel. Subsequent propagation introduces the curvature effect, causing λ to gradually diminish along the radial direction. Given the earlier analysis, it is evident that λ serves as the characteristic parameter signifying the sensitivity of detonation, with an inverse correlation to the detonation strength. Around the 105° mark, the λ near the inner wall extends to about 4.1 mm, a value of 1.8 times larger than that within the straight channel operating under the same initial pressure. Conversely, the smallest λ near the outer wall reduces to nearly two-thirds of its original size. Afterward, λ experiences no further alterations. As the initial pressure diminishes to 45 kPa (Fig. 5b), the λ proximal to the inner wall continues to increase and ultimately vanishes around the 155° point. This phenomenon emerges because near the inner wall the detonation wave front encounters a critical curvature that induces local quenching of the detonation. Consequently, the leading shock wave and the chemical reaction front disengage within this specific zone. However, at this juncture, the transverse wave originating from the outer wall ignites the unburnt mixture within the decoupling zone (which is pre-compressed by the leading shock wave). This process gives rise to a band of cellular structures extending from the outer to inner wall. In proximity to the inner wall, the regenerative detonation is overdriven, leading to the production of finer cellular structures. Upon further reduction in the initial pressure to 30 kPa (Fig. 5c), the observations indicate the presence of cellular structures near the outer wall, characterized by smaller sizes as compared to λ within the straight channel. Additionally, the width of the region housing these cellular structures remains consistent along the radial direction. In [35] detailed numerical simulations were carried out to elucidate the morphology of these cellular structures. The findings revealed that this morphology arises from a stable detonation-shock front configuration. The stable configuration typically features a broad curved wave originating at the inner wall, often connected to the outer wall boundary by means of the stable Mach stem. The measured cellular structures from experiments indicate that when the initial pressure is higher than 50 kPa, the detonation wave can propagate with a stable wave-front within the annular channel.

In Fig. 6 we have numerically calculated the pressure contours for the detonation flow field at various instances, all under the initial pressure of 60 kPa. In each image, the red curves superimposed represent the chemical reaction surface (depicted by 99% reactant depletion contours). An analysis of Fig. 6 reveals that, in proximity to the inner wall, the leading shock front detaches from the chemical reaction surface. Along the radial direction, the distance between the leading shock and the chemical reaction zone gradually diminishes, indicating a progressive surge in the detonation wave strength. Additionally, it is apparent that the spacing of transverse waves near the inner wall significantly surpasses that observed near the outer wall. Notably again, the maximum spacing between adjacent transverse waves dictates the cellular width, and inversely correlates with the detonation strength (λ). The growing gap between the leading shock front and the chemical reaction surface near the inner wall results in the emergence of a substantial zone filled with the unburned mixture. This phenomenon is particularly pronounced when the mixture sensitivity declines or the divergence effect of the inner wall amplifies. Activation occurs in the unburned mixture as the Mach reflection of the transverse wave emanating from the inner wall generates the elevated temperature and pressure levels. Consequently, the transverse wave reflects off the inner wall surface and subsequently propagates toward the outer wall. In the neighborhood of the outer wall, where the geometrical compression effects maintain the state of overdriven detonation, the close coupling of the chemical reaction front to the shock wave serves as compelling evidence.

The inherent instability of the detonation wave becomes evident through interactions between the triple points that lead to an unstable pressure and velocity distributions along the wave front. Figure 7 numerically graphically displays the evolution of the velocity and the pressure at various locations within

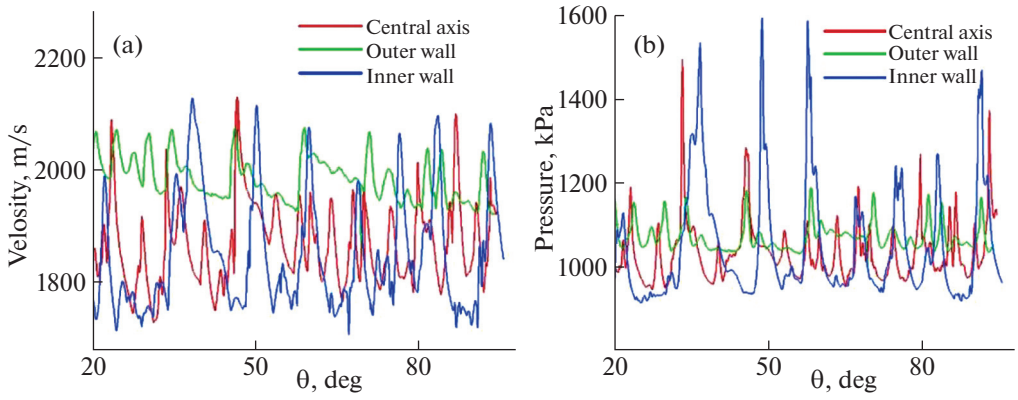

Fig. 7. Numerical simulation of the evolution of the velocity and the pressure in the annular channel: velocity (a) and pressure (b).

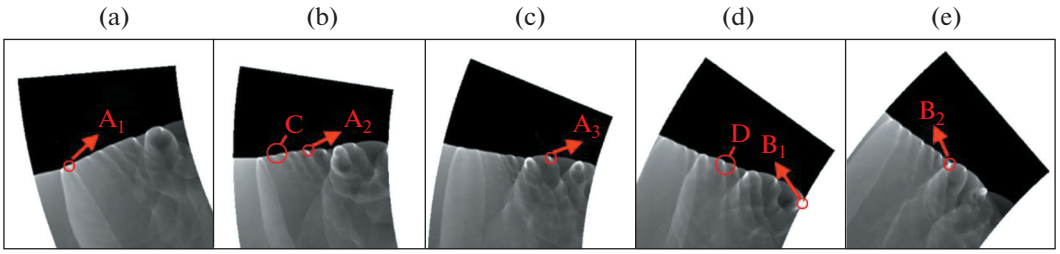

Fig. 8. Evolution of a triple point along the detonation wave front during a single cycle obtained by numerical simulation.

the annular channel. The vertical axes show the velocity and the pressure, while the horizontal axes correspond to the circumferential angle of the annulus. When considering Fig. 7, it is apparent that both the velocity and the pressure associated with the detonation wave undergo substantial periodic oscillations. In the radial motion, the velocity and pressure amplitudes arrange themselves in decreasing order of magnitude namely, the inner wall, the central axis, and the outer wall. This arrangement stems from occurrence of the Mach reflection, facilitated by the interaction of transverse waves with the inner wall. This interaction ignites the nearby unburned mixture, resulting in the instantaneous release of significant chemical energy. Consequently, there is a rapid surge in the pressure that drives a pronounced increase in the detonation wave velocity. In the neighborhood of the outer wall, the detonation wave remains consistently overdriven, with its leading shock directly igniting the mixture in its path. Since the region of unburned gas between the leading shock and the chemical reaction surface remains relatively small, the fluctuations in energy release are comparatively mild. As a result, this leads to the minimum pressure and velocity amplitudes. On the central axis of the channel, the competing effects of divergence and compression from the inner and outer walls form the dynamic balance. In essence, once this equilibrium is achieved, the magnitudes of the pressure and velocity fluctuations align with those observed in the straight channel. Moreover, the average velocity and pressure follow a descending order of magnitude, namely, the outer wall, the central axis, and the inner wall. To ensure stable and self-sustaining propagation of the detonation wave with a uniform rotational angular velocity, it is imperative that the linear velocity of the detonation wave front along the radial direction increases continually. These dynamics are facilitated by the substantial chemical reaction release near the outer wall, that ensures the sustained propagation of overdriven detonation which attains the highest value of the average pressure.

Figure 8 numerically depicts the interaction of triple points along the detonation front, illustrating the process of pressure oscillation within a single cycle. Initially, triple point A_1 moves from the outer wall toward the inner wall. It undergoes continuous collisions with the triple points traveling in the opposite direction, leading to gradual increase in the pressure from 1150 to 1280 kPa (at A_2). In proximity to the inner wall, where the shock wave disengages from the chemical reaction surface, the effective collisions are limited, causing a decrease in the strength. Consequently, the pressure experiences a reduction to 965 kPa (at A_3). The triple points are further weakened or even eradicated by rarefaction waves originating

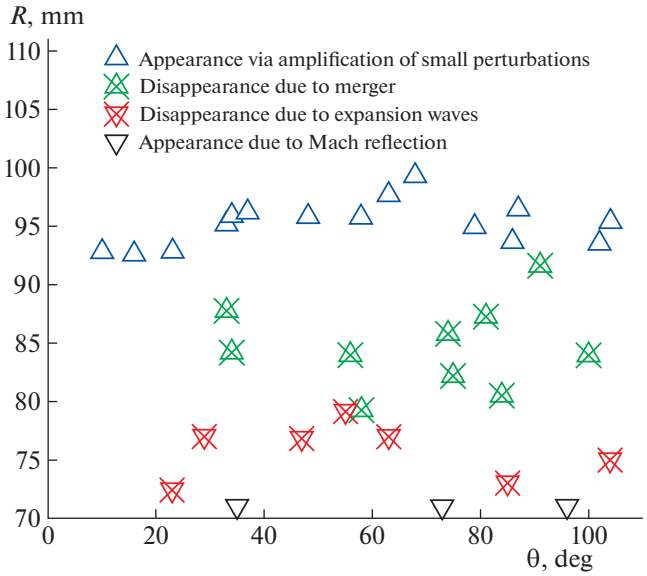

Fig. 9. Location for generation and disappearance of triple points along the detonation front by obtained numerical simulation.

from the inner wall. After the transverse shock wave collides with the inner wall surface, the resulting high temperature and pressure ignite the unburned mixture, leading to a rapid pressure surge. This sequence culminates in the pressure peak of 1435 kPa. This collision, recognized as a strong Mach reflection event, can initiate a new triple point (B_1) that progresses toward the outer wall. As the triple point advances to the outer wall, it continuously collides with others, maintaining the pressure stability around 1200 kPa (at B_2). Subsequent to the collision with the outer wall, the cycle recommences. Importantly, near the outer wall, small perturbations on the Mach wave intensity can gradually amplify, ultimately forming new triple points (area C). Additionally, strong triple points have the capacity to engulf weaker ones, leading to reduction in their number (area D).

The presence of the triple points serves as the crucial indicator of consistent propagation of the detonation wave. Figure 9 visually illustrates the points at which triple points emerge and vanish along the detonation front within the annular channel. In this figure, the horizontal coordinate corresponds to the circumferential angle, while the vertical coordinate depict the radial distance extending from the inner wall towards the outer wall. When observing the figure, it becomes apparent that both the inner and outer walls can give rise to new triple points. In proximity to the outer wall, the amplification of minor disturbances facilitates the formation of triple points moving towards the inner wall. Conversely, near the inner wall, periodic occurrence of triple points is attributed to Mach reflection that directs them towards the outer wall. The expansion waves stemming from the inner wall have the potential to weaken the intensity of detonation wave. Consequently, within this region the triple points tend to diminish or even dissipate, comparable to the effect of an acoustic absorption wall. Another scenario emerges when two adjacent triple points collide, potentially leading to their merger and a subsequent reduction in the overall number of triple points. This phenomenon is most prominent in the vicinity of the annulus' axis. Overall, the cyclical appearance and disappearance of triple points across the entire wave front sustain equilibrium. This dynamic equilibrium is instrumental in ensuring that the detonation wave maintains a consistent velocity throughout the annular channel.

SUMMARY

The present study presents a comprehensive exploration of the characteristics of steady detonation wave propagation within an annular channel, utilizing a combination of experimental and numerical investigations. Employing the two-dimensional Euler equations coupled with detailed finite-rate chemistry, numerical simulations were carried out using the fifth-order weighted essentially non-oscillatory (WENO) scheme and the semi-implicit Runge–Kutta method. The experiments were analyzed by means

of observations of the cellular structures imprinted on soot-coated stainless steel plates. This leads to the following key conclusions:

1. **Non-uniform detonation front strength:** The curvature of the annular channel introduces geometric effects that render the detonation front strength uneven. As the radial direction is traversed, the average velocity of the detonation wave progressively increases. However, the circumferential angular velocity remains relatively constant. This balance in the angular velocity facilitates the sustained and stable propagation of the detonation wave along the annular channel.

2. **Oscillatory behavior of the detonation wave:** Periodic oscillations in the propagation speed and pressure are observed near the inner wall of the annular channel. These fluctuations can be attributed to the alternating enhancement and weakening of the detonation wave, primarily driven by the intense heat release from the unburned mixture close to the inner wall. The resulting variations in the heat and pressure generate the observed oscillations in the wave's behavior.

3. **Role of triple points:** The presence and the behavior of triple points hold paramount significance in understanding the steady propagation of the detonation wave. While most triple points are generated near the outer wall due to amplification of small perturbations, some are produced through Mach reflections on the inner wall. Occasional collisions between the neighboring triple points can lead to their fusion, resulting in decrease in their number. Moreover, the influence of the expansion waves from the inner wall can either attenuate or eliminate the triple points. The constant number of triple points along the wave front emerges as the key factor in maintaining the wave's steady propagation.

In essence, this paper contributes to the deeper understanding of detonation wave dynamics within the annular channels, uncovering the interplay of geometric effects, heat release, and triple point interactions. The combination of experimental insights and numerical simulations provides a comprehensive view of the complex phenomena involved in the steady detonation wave propagation. These findings not only enhance our knowledge of combustion dynamics but also offer valuable insights for the design and optimization of systems relying on controlled detonation processes, with potential implications for advancements in energy production and utilization.

FUNDING

This work was supported by the National Natural Science Foundation of China under Grant no. 51876084.

CONFLICT OF INTEREST

The authors of this work declare that they have no conflicts of interest.

REFERENCES

1. Smirnov, N.N., Nikitin, V.F., Stamov, L.I., Mikhalchenko, E.V., and Tyurenkova, V.V., Rotating detonation in a ramjet engine three-dimensional modeling, *Aerosp. Sci. Technol.*, 2018, vol. 81, pp. 213–224.
2. Smirnov, N.N., Nikitin, V.F., Stamov, L.I., Mikhalchenko, E.V., and Tyurenkova, V.V., Three-dimensional modeling of rotating detonation in a ramjet engine, *Acta Astronaut.*, 2019, vol. 163, pp. 168–176.
3. Betelin, V.B., Nikitin, V.F., and Mikhalchenko, E.V., 3D numerical modeling of a cylindrical RDE with an inner body extending out of the nozzle, *Acta Astronaut.*, 2020, vol. 176, pp. 628–646.
4. Nikitin, V.F. and Mikhalchenko, E.V., Safety of a rotating detonation engine fed by acetylene–oxygen mixture launching stage, *Acta Astronaut.*, 2022, vol. 194, pp. 496–503.
5. Shepherd, J.E., Structural response of piping to internal gas detonation, *J. Pressure Vessel Technol.*, 2009, vol. 131, no. 3, pp. 031204.
6. Uchida, M., Suda, T., Fujimori, T., and Inagaki, T., Pressure loading of detonation waves through 90-degree bend in high pressure $H_2-O_2-N_2$ mixtures, *Proc. Combust. Inst.*, 2011, vol. 33, no. 2, pp. 2327–2333.
7. Zhuravskaya, T.A. and Levin, V.A., Control of detonation wave in a channel with obstacles using preliminary gas mixture preparation, *Fluid Dyn.*, 2020, vol. 55, pp. 488–497.
8. Egoryan, A.D. and Kraiko, A.N., Comparison of air-breathing engines with slow and detonation combustion, *Fluid Dyn.*, 2020, vol. 55, pp. 264–278.
9. Pan, Z.H., Fan, B.C., Zhang, X.D., Gui, M.Y., and Dong G., Wavelet pattern and self–sustained mechanism of gaseous detonation, *Combust. Flame*, 2011, vol. 158, no. 11, pp. 2220–2228.
10. Melguizo-Gavilanes, J., Rodriguez, V., Vidal, P., and Zitoun, R., Dynamics of detonation transmission and propagation in a curved chamber: a numerical and experimental analysis, *Combust. Flame*, 2021, vol. 223, pp. 460–473.

11. Pan, Z.H., Zhang, Z.H., Zhang, P.G., and Zhu, M.H., Experimental investigation and comparison of flame acceleration, hot spot ignition, and initiation of detonation in curved and straight channels, *Combust. Flame*, 2022, vol. 242, pp. 112–154.
12. Tunik, Y.V., Numerical modeling of detonation combustion of hydrogen–air mixtures in a convergent-divergent nozzle, *Fluid Dyn.*, 2010, vol. 45, pp. 264–270.
13. Nakayama, H., Moriya, T., Kasahara, J., Matsuo, A., Sasamoto, Y., and Funaki, I., Stable detonation wave propagation in rectangular-cross-section curved channels, *Combust. Flame*, 2012, vol. 159, no. 2, pp. 859–869.
14. Xia, Z.J., Ma, H., Zhuo, C.F., and Zhou, C.S., Propagation process of H_2/air rotating detonation wave and influence factors in plane-radial structure, *Int. J. Hydrogen Energy*, 2018, vol. 43, no. 9, pp. 4609–4622.
15. Pan, Z.H., Qi, J., Pan, J.F., Zhang, P.G., Zhu, Y.J., and Gui, M.Y., Fabrication of a helical detonation channel: Effect of initial pressure on the detonation propagation modes of ethylene–oxygen mixtures, *Combust. Flame*, 2018, vol. 192, pp. 1–9.
16. Nakayama, H., Kasahara, J., Matsuo, A., and Funaki, I., Front shock behavior of stable curved detonation waves in rectangular-cross-section curved channels, *Proc. Combust. Inst.*, 2013, vol. 34, no. 2, pp. 1939–1947.
17. Lee, S.H., Jo, D.R., and Choi, J.Y., Effect of curvature on the detonation wave propagation characteristics in annular channels, *AIAA Paper*, 2008, p. 988.
18. Tunik, Y.V., Detonation combustion of hydrogen in a convergent-divergent nozzle with a central coaxial cylinder, *Fluid Dyn.*, 2014, vol. 49, pp. 688–693.
19. Li, J., Ning, J.G., Zhao, H., Hao, L., and Wang, C., Numerical investigation on the propagation mechanism of steady cellular detonations in curved channels. *Chin. Phys. Lett.*, 2015, vol. 32, no. 4, p. 048202.
20. Thomas, G. and Williams, R., Detonation interaction with wedges and bends, *Shock Waves*, 2002, vol. 11, no. 5, pp. 481–492.
21. Sugiyama, Y., Nakayama, Y., Matsuo, A., Nakayama, H., and Kasahara, J., Numerical investigation on detonation propagation in a two-dimensional curved channel, *Combust. Sci. Technol.*, 2014, vol. 186, pp. 1662–1679.
22. Zhang, X.D., Fan, B.C., Pan, Z.H., and Gui, M.Y., Experimental and numerical study on detonation propagating in an annular cylinder, *Combust. Sci. Technol.*, 2012, vol. 184, pp. 1708–1717.
23. Rodriguez, V., Jourdain, C., Vidal, P., and Zitoun, R., An experimental evidence of steadily-rotating overdriven detonation, *Combust. Flame*, 2019, vol. 202, no. 4, pp. 132–142.
24. Radulescu, M.I. and Lee, J.H.S., The failure mechanism of gaseous detonations: experiments in porous wall tubes, *Combust. Flame*, 2002, vol. 131, no. 1–2, pp. 29–46.
25. Nikitin, V.F., Mikhalchenko, E.V., Stamov, L.I., Tyurenkova, V.V., and Smirnov, N.N., Evolution of the cellular structure of detonation waves under the condition of non-uniform initiation, *Acta Astronaut.*, 2023, vol. 213, pp. 156–167.
26. Smirnov, N.N., Nikitin, V.F., Mikhalchenko, E.V., Stamov, L.I., and Tyurenkova, V.V., Modelling cellular structure of detonation waves in hydrogen–air mixtures, *Int. J. Hydrogen Energy*, 2023, in press. https://doi.org/10.1016/j.ijhydene.2023.08.184
27. Gordon, S. and McBride, D.J., A computer program for complex chemical equilibrium compositions–incident and reflected shocks and Chapman–Jouguet detonations, 1971, Report No. SP–273.
28. Jiang, G.S. and Shu, C.W., Efficient implementation of weighted ENO schemes. *J. Comput. Phys.*, 1996, vol. 126, no. 1, pp. 202–228.
29. Zhong, X.L., Additive semi-implicit Runge–Kutta methods for computing high-speed nonequilibrium reactive flows, *J. Comput. Phys.*, 1996, vol. 128, no. 1, pp. 19–31.
30. Smirnov, N.N., Betelin, V.B., Nikitin, V.F., Stamov, L.I., and Altoukhov, D.I., Accumulation of errors in numerical simulations of chemically reacting gas dynamics, *Acta Astronaut.*, 2015, vol. 117, pp. 338–355.
31. Smirnov, N.N., Betelin, V.B., Shagaliev, R.M., Nikitin, V.F., Belyakov, I.M., Deryuguin, Y.N., Aksenov, S.V., Korchazhkin, D.A., Stamov, L.I., and Altoukhov, D.I., Hydrogen fuel rocket engines simulation using LOGOS code, *Int. J. Hydrogen Energy*, 2014, vol. 39, pp. 10748–10756.
32. Oran, E.S., Weber, Jr.J.W., Stefaniw, E.I., Lefebvre, M.H., and Anderson, Jr.J.D., A numerical study of a two-dimensional H_2–O_2–Ar detonation using a detailed chemical reaction model, *Combust. Flame*, 1998, vol. 113, nos. 1–2, pp. 147–163.
33. Oran, E.S., Young, T.R., Boris, J.P., and Cohen, A., Weak and strong ignition. I. Numerical simulations of shock tube experiments, *Combust. Flame*, 1982, vol. 48, pp. 135–148.
34. Eckett, C.A., Numerical and analytical studies of the dynamic of gaseous detonation, 2001, CA, USA: California Institute of Technology.
35. Short, M., Chiquete, C., and Quirk, J., Propagation of a stable gaseous detonation in a circular arc configuration, *Proc. Combust. Inst.*, 2019, vol. 37, no. 3, pp. 3593–3600.